Journal of Marine Science and Application (2025) 24: 1103-1114
https://doi.org/10.1007/s11804-025-00668-7

RESEARCH ARTICLE

Numerical Investigation on the Effect of Material Inhomogeneity of Welded Joints on the Local Stress and Strain

Yan Dong[1,2,3], Zhihao Ai[1] and Lingsu Liu[1]

Received: 07 August 2024 / Accepted: 07 September 2024

Abstract
Welded joints can be divided into different material zones, with considerable variation of material properties around the weld toe. The material inhomogeneity influences the local stress and strain of welded joints under monotonic and cyclic loading. This study aims to examine the local stress and strain characteristics of welded joints considering material inhomogeneity. Numerical models with various material zones were developed, and material properties were determined based on hardness. Smooth specimen models were used to analyze stress and strain distributions excluding notch effects. A detailed inhomogeneous model of a welded joint was established based on extensive microhardness measurements around the weld toe and the Kriging interpolation method. Additionally, a homogeneous model and a simplified inhomogeneous model, based on limited measured data, were generated and compared with the detailed inhomogeneous model. Fatigue life was estimated using the Smith, Watson, and Topper method based on the obtained stress and strain. For smooth specimen models, stress concentration occurs at a location where the strain is not significant, and fatigue cracks were most likely to initiate from the base metal. Results from the two simplified models showed deviations from those of the detailed inhomogeneous model, and the limitations of these simplified models are discussed.

Keywords Material inhomogeneity; Welded joints; Hardness; Local stress and strain

1 Introduction

Conventional arc welding processes are widely used across various industries, including marine applications, to join steel plates and fabricate steel structures (Ezer and Çam, 2022; Şenol and Çam, 2023; Serindağ and Çam, 2022; Serindağ et al., 2022; Serindağ and Çam, 2023; Serindağ and Çam, 2021). The welding process can introduce unfavorable welding defects, discontinuities, and residual stresses, which often lead to the emergence of fatigue cracks from the welded joints rather than from the steel plates when the welded structures are subjected to cyclic loading. Various approaches for assessing the fatigue strength of welded joints have been developed (Radaj et al., 2006). However, most of these approaches are only applicable to high cycle fatigue (HCF), and they typically overlook the influence of material proper-ties on the fatigue strength of steel welded joints (Hobbacher, 2015). Studies have shown that the tensile strength of the material has a negligible effect on the fatigue strength of welded joints with relatively sharp notches in the HCF regime (Maddox, 1991). This effect may be attributed to the dominance of the fatigue crack propagation life on the fatigue life of welded joints with sharp notches and the minimal influence of the microstructures within whole material classes, such as steels, on the crack propagation behavior in the Paris regime (Dong et al., 2022; Kucharczyk et al., 2018).

Material inhomogeneity in microstructure and mechanical properties is a typical characteristic of welded joints. A welded joint comprises weld metal (WM), heat-affected zone (HAZ), and base metal (BM), with the HAZ further divided into distinct subzones (Easterling, 2013). The effect

Article Highlights

- The study investigates the impact of material inhomogeneity on stress and strain response in welded joints under various loading conditions.
- Microhardness combined with Kriging interpolation is employed to establish a detailed inhomogeneous model for accurate local stress-strain and fatigue life estimation of welded joints.
- Simplified models lead to notable deviations from the results of the detailed model, highlighting the limitations of these models.

✉ Yan Dong
yan.dong@hrbeu.edu.cn

[1] Yantai Research Institute of Harbin Engineering University, Harbin Engineering University, Yantai 264000, China

[2] College of Shipbuilding Engineering, Harbin Engineering University, Harbin 150001, China

[3] HEU-UL International Joint Laboratory of Naval Architecture and Offshore Technology, Harbin 150001, China

of material properties on fatigue life is particularly evident in the low cycle fatigue (LCF) regime (Dong et al., 2017; Remes, 2008; Saiprasertkit et al., 2012; Tsutsumi et al., 2022). When estimating local stresses, strains, and fatigue life, the material properties at the crack initiation site are typically considered. Fatigue cracks in welded joints often initiate from the HAZ or the WM. Therefore, in the LCF assessments, the material properties of the HAZ or WM, rather than the BM, are typically applied. In addition, the effect of materials on fatigue life is evident for high-quality welded joints, where the fatigue crack initiation life cannot be neglected. In detailed fatigue life estimations for high-quality welded joints based on fracture mechanics, the material properties of the HAZ, rather than the BM, provide a superior approximation of the experimental fatigue lives in the HCF regime (Madia et al., 2018). Furthermore, after pre-welding or post-welding heat treatment of the welded joint, the material properties of the HAZ are improved, resulting in a joint with a longer fatigue life than the typical as-welded state (Mallieswaran et al., 2023; Rajendran et al., 2022; Venkataramanan et al., 2022). This feature highlights the crucial role of the material.

The underlying assumption of using the material properties of the crack initiation site is that the welded joint is homogeneous and behaves similarly to the material at that site. While this assumption has been validated in numerous studies, the inhomogeneous nature of welded joints is not considered. Research has shown that, under extremely high monotonic or cyclic loading, local stresses and strains cannot be accurately predicted using the material properties of the crack initiation site (Dong et al., 2017). Additionally, the use of a homogeneous model can result in inaccurate predictions of local strain distributions, as presented by Tsutsumi et al. (2022).

In recent years, the finite element method (FEM) has been employed in some studies to model the various material zones of welded joints, allowing for a more accurate consideration of material inhomogeneity and its effect on fatigue behavior. Table 1 presents a summary of these studies. The finite element models are generally divided into three zones. HAZ is further divided into several subzones due to the considerable variation in microstructure and material properties. While the material properties of the WM and BM can be determined through testing, those of the HAZ are difficult to measure directly due to their small dimensions, making it challenging to prepare test specimens. Heat treatment of BM specimens is performed to reproduce the conditions of the HAZ specimen. Alternatively, using empirical equations that correlate material properties with measurable quantities, such as hardness, can be used to estimate the material properties of different zones.

The FEM with different material zones was also used to analyze the fracture behavior of spot-welded joints (Yao et al., 2023). Uniaxial tensile tests were conducted on spot-welded advanced high-strength steel, and local mechanical properties were assessed through indentation and miniaturized tensile tests. The correlations between these properties were quantified, and FEM models were established based on these correlations. The fracture behaviors of different spot-welded joints were simulated using the modified Mohr–Coulomb model.

The finite element models used in the aforementioned studies represent simplified versions of real-life conditions. Typically, these models are established using limited experimental data and several material zones. While these models are considered good approximations, their performance has not been extensively evaluated. Developing highly realistic models is necessary to effectively under-

Table 1 Some inhomogeneous finite element models employed in previous studies

Year	Reference	Structure model	Material properties
2008	Remes (2008)	Butt-welded joint with four material zones: BM, TZ* (four subzones), HAZ (four subzones), WM	BM and WM determined by tests Others determined by interpolation based on the hardness distribution
2009	Wang and Shang (2009)	Spot-welded joint with six zones: BM, weld nugget, four HAZs	Derived based on BM according to the hardness distribution
2012	Saiprasertkit et al. (2012)	Load-carrying cruciform joints with three material zones: BM, HAZ, WM	BM and WM determined by testing HAZ derived from BM
2017	Dong et al. (2017)	Butt-welded joint with three material zones: BM, HAZ (six subzones), WM	Derived based on the hardness value of different zones
2022	Tsutsumi et al. (2022)	Butt-welded joint with seven material zones	Determined by tests of heat-treated round bar specimens
2022	Xu et al. (2022)	Round bar specimen from butt-welded joints, three zones: WM, HAZ (four subzones), BM	BM and WM determined by tests Others determined based on the hardness distribution
2023	Wang et al. (2023)	Rib-to-deck welded joint with three material zones: BM, HAZ, WM	BM, WM, and HAZ calibrated by test data

Note: *TZ is the transition zone.

stand the local stress and strain characteristics of welded joints under substantial monotonic or cyclic loading, as well as to evaluate the accuracy of simplified models based on limited data.

The material inhomogeneity of welded joints is crucial to the LCF regime. In previous studies on the fatigue strength assessment of welded joints under high cyclic loading, homogeneous and simplified inhomogeneous models have been employed to calculate local stresses and strains. However, the performance of these models has not been extensively evaluated. The present study mainly aims to assess their performance by comparing them with a highly detailed inhomogeneous model. Based on the findings, some recommendations will be provided for evaluating local stresses and strains in the LCF regime.

In the present study, a numerical investigation is conducted to examine the effect of material inhomogeneity in welded joints on local stress and strain under substantial monotonic or cyclic loading. Empirical equations correlating material properties and hardness are introduced. Smooth specimens, artificially divided into various material zones, are analyzed to investigate the characteristics of stress and strain, excluding the notch effect. A detailed inhomogeneous model of a welded joint, based on intensive microhardness measurements around the weld toe and the Kriging interpolation method, is constructed to determine local stresses and strains. A homogeneous model and a simplified inhomogeneous model are also analyzed, with their compared to those obtained from the detailed inhomogeneous model. The limitations of the two simplified methods are discussed. Finally, the fatigue lives of the smooth specimen and the welded joint are both evaluated.

2 Material properties based on hardness

Although experimental methods are available, simplified methods based on hardness are used in the present study to determine the material properties of different zones. This approach is adopted because the hardness can easily be measured and is more useful for practical applications. Numerous empirical equations that describe the correlation between material properties and hardness have been developed from extensive experimental data on different materials (Lopez and Fatemi, 2012; Pavlina and Van Tyne, 2008).

The relationship between hardness and monotonic yield stress is proposed as follows (Lopez and Fatemi, 2012):

$$\sigma_y = 3.9 \cdot 10^{-3}\mathrm{HB}^2 + 1.62\mathrm{HB} \tag{1}$$

where σ_y is the monotonic yield stress, and HB is the Brinell hardness.

The cyclic material behavior is characterized by the cyclic strength coefficient K' and strain hardening exponent n' and can be described using the Ramberg–Osgood equation:

$$\varepsilon_a = \frac{\sigma_a}{E} + \left(\frac{\sigma_a}{K'}\right)^{\frac{1}{n'}} \tag{2}$$

where ε_a and σ_a are the amplitude of true strain and stress, respectively, and E is the Young's modulus.

The K' can be estimated as follows (Basan et al., 2010):

$$K' = 0.009\mathrm{HB}^2 + 0.117\,3\mathrm{HB} + 376.75 \tag{3}$$

The estimation of n' can be realized using the following (Lopez and Fatemi, 2012):

$$n' = -0.37\log\left(\frac{\sigma_y'}{K'}\right) \tag{4}$$

$$\sigma_y' = 2.5 \cdot 10^{-3}\mathrm{HB}^2 + 1.49\mathrm{HB} \tag{5}$$

where σ_y' is the cyclic yield stress.

The monotonic material behavior can also be described by the Ramberg–Osgood equation, but K' and n' are replaced by the monotonic strength coefficient K and monotonic strain hardening exponent n, respectively. The monotonic parameters are correlated with the cyclic ones (Lopez and Fatemi, 2012), and the following empirical equations can be used:

$$K' = K \tag{6}$$

$$n' = 0.64n + 0.07 \tag{7}$$

Vickers hardness may be measured; thus, a transformation between the Vickers hardness and Brinell hardness can be performed using (Remes et al., 2012):

$$\mathrm{HB} = 0.980\,1 \cdot \mathrm{HV}^{0.994\,1} \tag{8}$$

where HV is the Vickers hardness.

The fatigue properties of the material can also be derived from the hardness. The Smith, Watson, and Topper (SWT) model (Smith, 1970) is typically used in fatigue life estimation:

$$\sigma_{1,\max}\frac{\Delta\varepsilon_1}{2} = \frac{\sigma_f'^2}{E}\left(2N_f\right)^{2b} + \sigma_f'\varepsilon_f'\left(2N_f\right)^{b+c} \tag{9}$$

where σ_f' is the fatigue strength coefficient, b is the fatigue strength exponent, ε_f' is the fatigue ductility coefficient, c is the fatigue ductility exponent, N_f is the number of cycles to fatigue failure, $\Delta\sigma_1$ is the principal strain range, and $\sigma_{1,\max}$ is the maximum stress on the principal strain range plane. The relationships between the fatigue property and the hardness are shown in Table 2 (Roessle and Fatemi, 2000).

Table 2 Fatigue properties (Roessle and Fatemi, 2000)

Fatigue properties	Equations
fatigue strength coefficient σ_f'	4.25HB + 225
fatigue strength exponent b	−0.09
fatigue ductility coefficient ε_f'	$(0.32\text{HB}^2 - 487\text{HB} + 191\,000)/E$
fatigue ductility exponent c	−0.56

3 Smooth specimen model

In welded joints, local stresses and strains are substantially influenced by notches, such as weld toes. Therefore, examining the characteristics of stress and strain distributions in smooth specimens with different material zones while excluding the effects of notches is necessary. This examination allows the isolation of the effect of material inhomogeneity alone. In practice, the smooth specimen corresponds to a butt weld that has been ground flush with the plate. In this section, smooth specimens, artificially divided into various material zones, are evaluated using FEM. The resulting elastic–plastic stress and strain distributions along the surface of the specimens are then obtained and analyzed.

The smooth specimen is assumed to be manufactured from a welded joint, with the excess WM removed, as shown in Figure 1. The thickness of the specimen is t. The specimen comprises three material zones, and the length of each zone is L, B, and L.

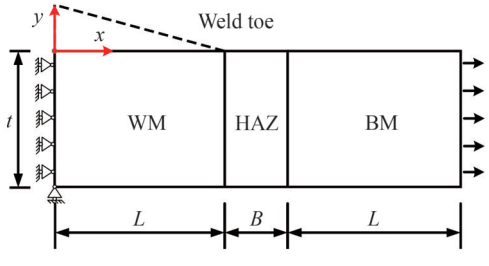

Figure 1 Geometry of smooth specimens

Finite element analysis is conducted using ANSYS (ANSYS, 2012). The plane stress cross-sectional models with the element type PLANE182 are used because the smooth specimens under uniaxial loading are generally in a plane stress state. The dimensions of the specimen are as follows: t = 5 mm, L = 5 mm, and B = 2 mm. The mesh size is 0.1 mm, according to a convergent study. The Young's modulus of $E = 2.06 \times 10^5$ MPa and Poisson's ratio of ν = 0.3 are used for the elastic material behavior. The multilinear elastic–plastic material model with a kinematic hardening rule and von Mises yield criterion is used, which is a close approximation of the Ramberg–Osgood equation. The boundary conditions are shown in Figure 1. Monotonic and cyclic loads are both considered in the analyses. For the cyclic load, a three-time-step analysis is conducted to obtain the stress–strain hysteresis loop, in which the remote stress at times 1, 2, and 3 are σ, $-\sigma$, σ, respectively.

Various material conditions are considered in this study. The BM is assumed to have a monotonic yield stress of $\sigma_{y,\text{BM}}$ = 315 MPa. The yield stress of WM is assumed to be 1.2, 1.3, and 1.4 times that of the BM, corresponding to mismatch ratios of 1.2, 1.3, and 1.4, respectively. The HAZ is further divided into several subzones, with the hardness of each HAZ subzone obtained through linear interpolation based on the hardness values of BM and WM. The hardness values for the BM and WM are derived in accordance with Eq. (1). The hardness declines linearly from the boundary between the WM and HAZ from the boundary between the HAZ and BM. The hardness at the center of each HAZ subzone can be calculated using the linear equation. The monotonic and cyclic stress–strain curves for each zone or subzone can be derived based on their corresponding hardness values using the equations introduced in Section 2. The monotonic and cyclic stress–strain curves for BM are shown in Figure 2(a), and a typical stress–strain history (i.e., hysteresis loop) for cyclic loading is shown in Figure 2(b). The relationship between the stress amplitude σ_a and strain amplitude ε_a is demonstrated by the cyclic stress–strain curve.

The assumed hardness distribution is approximately con-

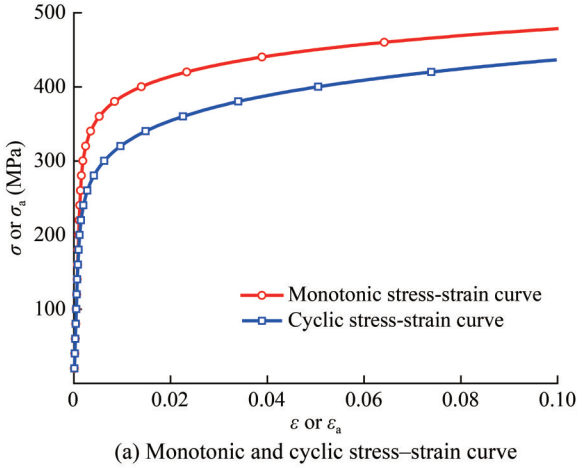

(a) Monotonic and cyclic stress–strain curve

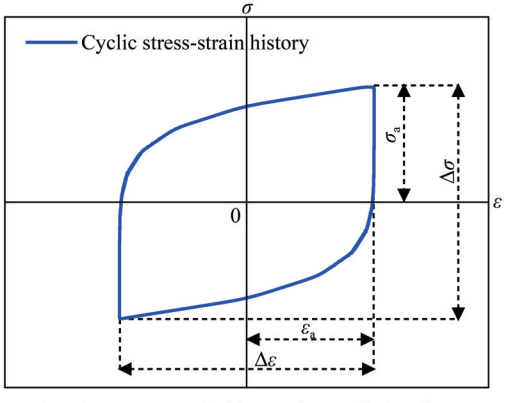

(b) The stress–strain history for cyclic loading

Figure 2 Material properties for BM

sistent with the measured hardness distribution provided in the following section, indicating that the monotonic and cyclic yield strength of the HAZ is higher than that of the BM. Kucharczyk et al. (2018) investigated the material properties of different material zones in thermally treated high-tensile steel specimens, and their results indicated that the monotonic and cyclic yield strength of the HAZ was higher than that of the BM. Notably, the yield strength of the HAZ is generally considered lower than that of the BM for high-tensile steels in ultimate strength assessments (Paik and Sohn, 2012). Further clarification may be needed on whether the HAZ experiences softening or hardening.

The applied monotonic load is equal to $\sigma_{y,\mathrm{BM}}$. The stress and strain distribution along the upper surface of the specimen, i.e., the x axis, is obtained. The stress and strain in the x direction are normalized based on the applied load. Figure 3 shows the effect of mismatch ratios on the stress and strain distribution. Notably, considering the stress distribution from the WM to BM, the stress increases to a maximum near the HAZ and then decreases to a minimum near the BM, close to the HAZ.

The maximum stress around the HAZ can be attributed to the increase in strain within WM, thereby also raising the stress. Although the strain increases within the HAZ, the stress can decrease due to the lower stress–strain curve material of the HAZ than that of the WM, leading to maximum stress. The strain continues to increase from WM to BM. Some fluctuations occur at the boundary of material zones. An existing local extreme of the strain at the BM close to the HAZ can be attributed to the lowest stress–strain curve of the BM material. The local peak occurrence of the strain ensures consistent stress at the material boundary. The mismatch ratio controls the stress and strain distribution within the HAZ. The stress within the HAZ and the maximum stress increase with the mismatch ratio, while the strain within the HAZ decreases with the mismatch ratio.

Figure 4 shows the results corresponding to the conditions where the yield stress of the WM is 1.2 times that of the BM, and the HAZ is divided into $n_{\mathrm{HAZ}} = 1$–5 subzones. Notably, the number of subzones drastically affects the stress and strain distribution in the HAZ. The local fluctuations in stress and strain decrease with n_{HAZ}. Furthermore, a low n_{HAZ} does not effectively capture the maximum stress.

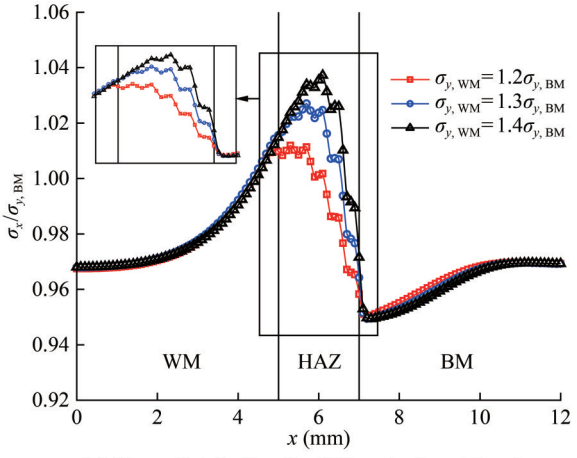

(a) Stress distribution for different mismatch rations

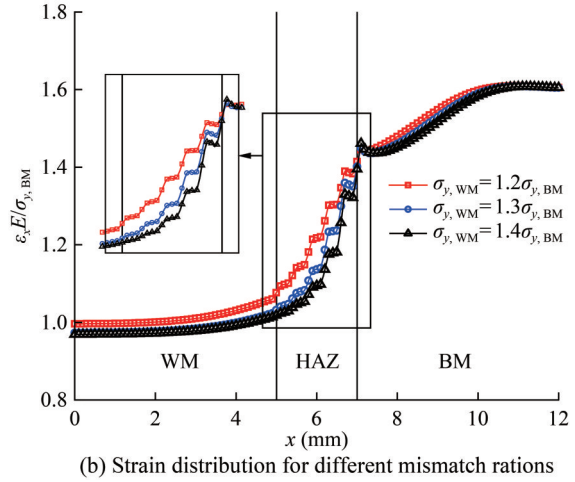

(b) Strain distribution for different mismatch rations

Figure 3 Stress-strain response for different mismatch ratios under monotonic load (number of HAZ subzones is 5)

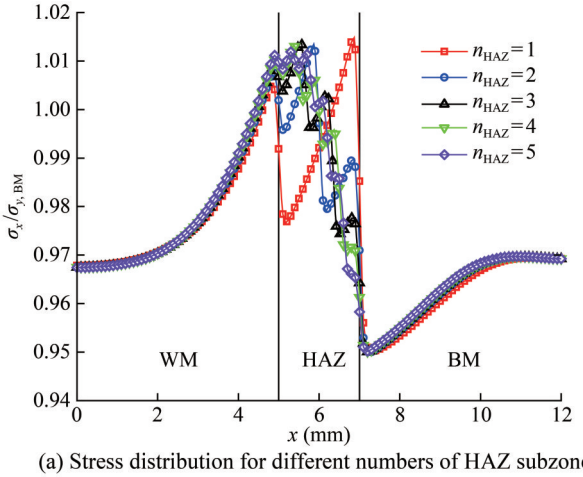

(a) Stress distribution for different numbers of HAZ subzones

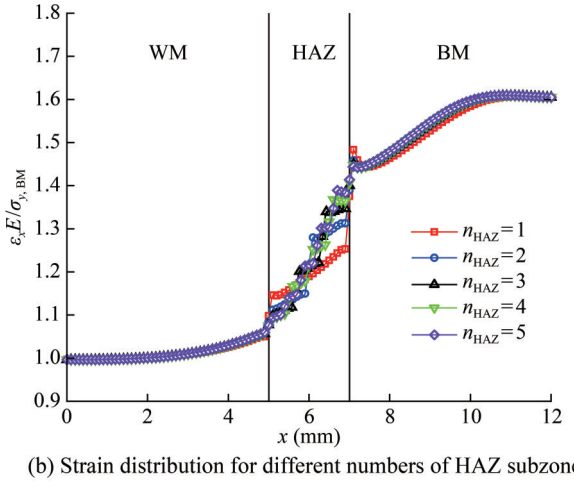

(b) Strain distribution for different numbers of HAZ subzones

Figure 4 Stress-strain response for different numbers of HAZ subzones under monotonic load ($\sigma_{y,\mathrm{WM}} = 1.2\sigma_{y,\mathrm{BM}}$)

The cyclic load is applied to the smooth specimen model, and the cyclic stress–strain curves are used. The load amplitude is also equal to the monotonic yield stress of the BM. The stress amplitude and plastic strain amplitude distributions for mismatch ratios of 1.2, 1.3, and 1.4 are shown in Figure 5. The plastic strain amplitude is considered because crack initiation generally occurs in areas where high cyclic plastic strain is observed (Besel et al., 2019).

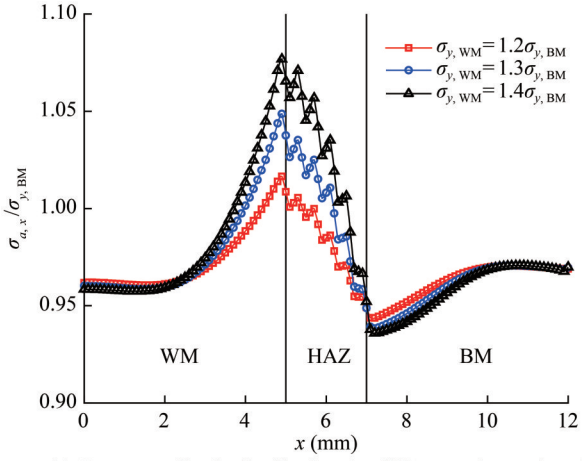

(a) Stress amplitude distribution for different mismatch ratios

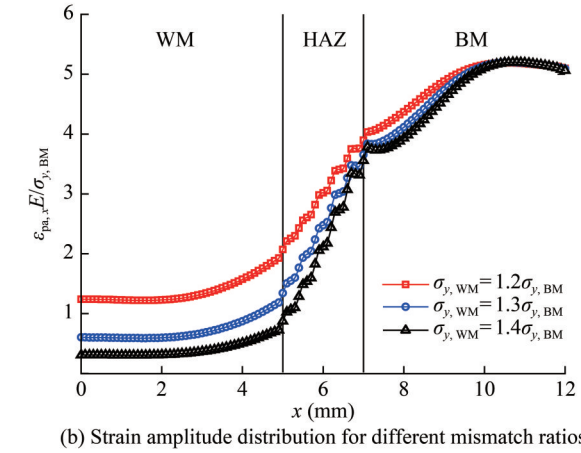

(b) Strain amplitude distribution for different mismatch ratios

Figure 5 Stress-strain response for different mismatch ratios under cyclic load (number of HAZ subzones is 5)

Figure 5 shows that the trends of stress amplitude and plastic strain amplitude are similar to those of stress and strain under monotonic loading. The plastic behavior is more noticeable than in the monotonic loading case. Maximum stresses are observed at the WM near the HAZ rather than within the HAZ. This finding indicates that although the strain in the HAZ is higher than in the WM, the stress decreases because the cyclic stress–strain curve of the HAZ is notably lower than that of the WM.

An existing stress concentration for the smooth specimen is attributed to material inhomogeneity. The stress concentration is expected to disappear when the cyclic load is sufficiently low, resulting in a specimen in the elastic domain. All the material zones have the same elastic material property. The stress concentration appears and increases with cyclic load. The increase in the mismatch ratio can also contribute to the rise in the stress concentration, as shown in Figure 5(a).

The maximum stress amplitude, which occurs around the HAZ on the smooth specimen surface, increases with the mismatch ratio due to material hardening around the HAZ. The plastic strain amplitude also continuously increases from the WM to the BM. However, as the mismatch ratio increases, the plastic strain amplitude of the WM decreases due to material hardening of the WM.

Notably, the location of stress concentration does not necessarily coincide with the fatigue crack initiation site, because the corresponding plastic strain amplitude is at a low level. If the plastic strain amplitude is the fatigue control parameter, then the BM may be the crack initiation site. In addition, the boundary between the HAZ and the BM may be dangerous. Despite the high plastic strain amplitude of the BM, micro defects and higher residual stress may exist at the boundary other than BM, increasing its fatigue tendency. The LCF of smooth specimens with various material zones should be monitored at multiple locations, which depends on the fatigue control parameter and the fatigue resistance of the location material.

4 Notched specimen model

Notched specimens, such as welded joints, are analyzed in this section to examine the effect of material inhomogeneity and stress concentration due to the notch. A more realistic finite element model for notch stress and strain analysis was developed based on measured microhardness around the weld toe and the Kriging interpolation method. Simplified finite element models were also used to assess the effect of various modeling options on the estimated notch stress and strain.

4.1 Hardness measurement

The microhardness around the weld toe of a fillet-welded T-joint was measured. Mild steel (AH32) with a thickness of 6 mm was used as the BM. Welding was performed using the GMAW process with TWE-711 wire. The geometry of the T-joint is shown in Figure 6(a). Wire electrode cutting was conducted to prepare the specimen for microhardness measurement. A Vickers microhardness tester was used, with a dwell time of 15 s and an applied load of 200 g. The measurements were taken in the shaded area, as shown in Figure 6(a). The origin of the coordinate is located at the weld toe. The distance between two measurement points along the x and y axes is 0.2 mm, and the indenter marks within the area are shown in Figure 6(b). The first

row of indenter marks beneath the BM surface is located at $y = -0.1$ mm.

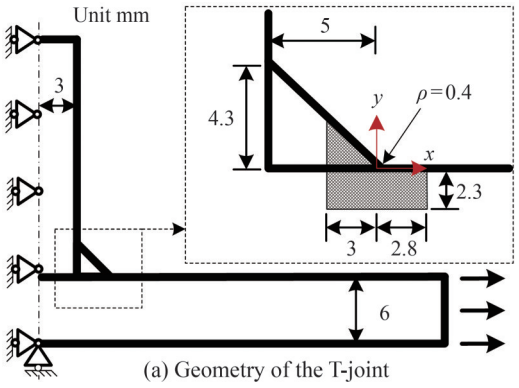

(a) Geometry of the T-joint

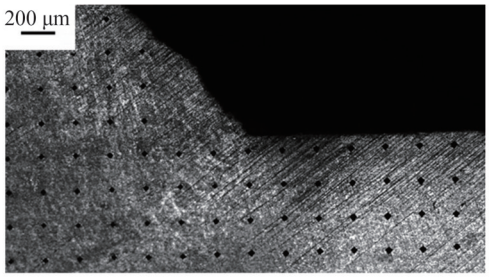

(b) Indenter marks for microhardness measurement

Figure 6 Microhardness measurement for notched specimens

The hardness distribution is shown in Figure 7. Notably, the three material zones, namely, WM, HAZ, and BM, are clearly distinguished. Local hardness peaks are randomly distributed within the WM, and the mean hardness of the WM is higher than that of the BM, indicating that the joint is overmatched. The weld toe is located at the boundary between the WM and the HAZ. The HAZ layer is thin, with a width of approximately 0.5–1 mm.

4.2 Detailed inhomogeneous model

Although the measurement points are relatively dense around the weld toe, the point results cannot be directly used for modeling the material properties in the finite element model. The Kriging interpolation method is employed to estimate the hardness at locations near the measurement points. The Kriging interpolation method was originally developed by Krige and then later expanded by Matheron (Matheron, 1973) for geostatistics. Important features of the Kriging method, such as its interpolation capability and flexibility to accurately approximate arbitrary functions, have been identified and applied in structural reliability analyses (Dong et al., 2020; Gaspar et al., 2014).

The finite element model of the T-joint, which is similar to that used in Section 3, is generated. The geometry and boundary conditions are shown in Figure 6(a). The weld toe radius is 0.4 mm, and the mesh size close to the weld toe is 0.01 mm, according to a mesh convergence study.

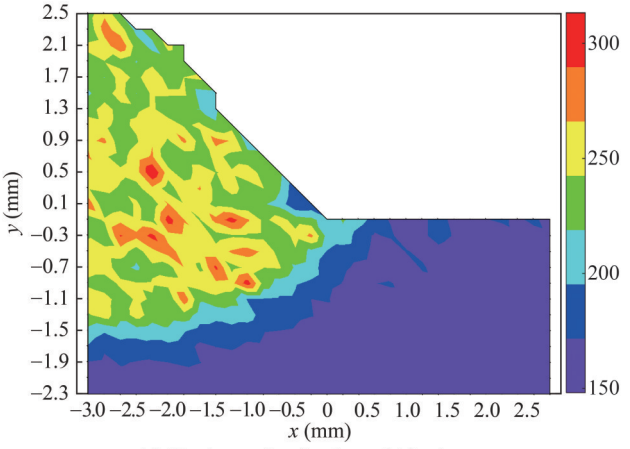

(a) Hardness distribution within the area

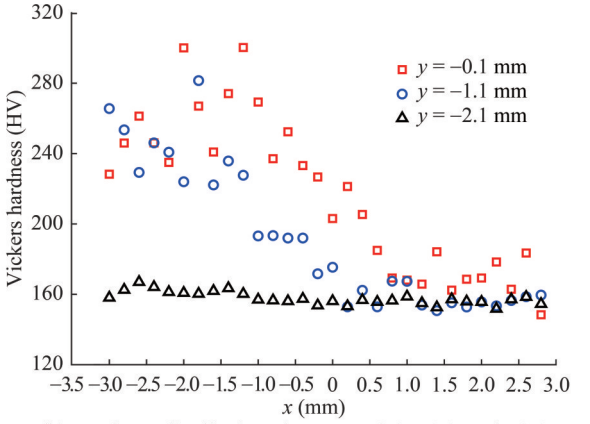

(b) Hardness distribution along $y = -0.1$, -1.1, and -2.1 mm

Figure 7 Hardness distribution around weld toe

The material properties of each element in the shaded area around the weld toe depend on the hardness of the location of the element centroid. A Kriging model is constructed based on the measured hardness and is used to predict the hardness at the element's centroid based on the coordinates of the centroid. The empirical equations introduced in Section 2 are then used to estimate the material properties of each element based on the hardness at the element's centroid. The material properties of elements located outside the shaded area are assumed to be those of the BM, with a Vickers hardness of 160. Macro files are developed to read the coordinates of each element's centroid and assign the estimated material properties to the element in the shaded area around the weld toe. The mesh configuration of the finite element model is shown in Figure 8.

The cyclic load is applied to the inhomogeneous model, and the principal stress amplitude and principal plastic strain amplitude along the weld toe surface are obtained. Figure 9 shows the results as a function of x for three cyclic loads with amplitudes of $0.8\sigma_{y,\mathrm{BM}}$, $0.9\sigma_{y,\mathrm{BM}}$, and $\sigma_{y,\mathrm{BM}}$, respectively. The origin of the coordinate system is also shown in the figure. The detailed inhomogeneous model is believed to produce highly reliable results because all the measured data are considered. The results from a homogeneous model

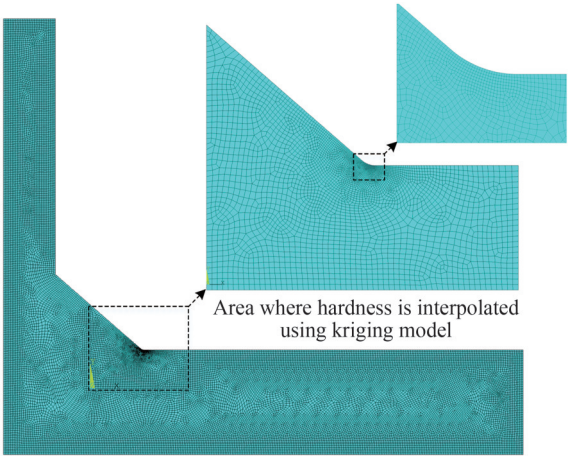

Figure 8 Mesh condition of the finite element model

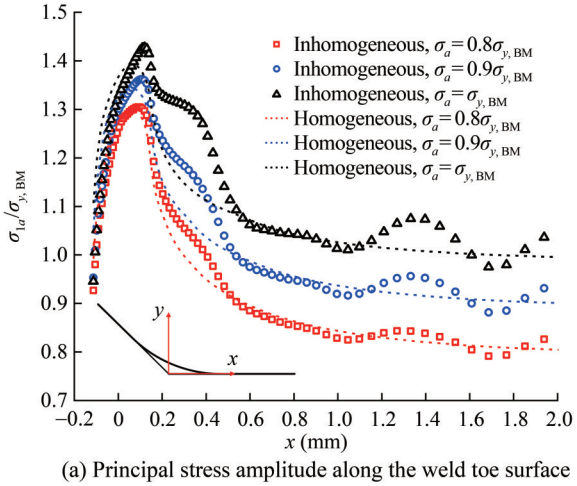

(a) Principal stress amplitude along the weld toe surface

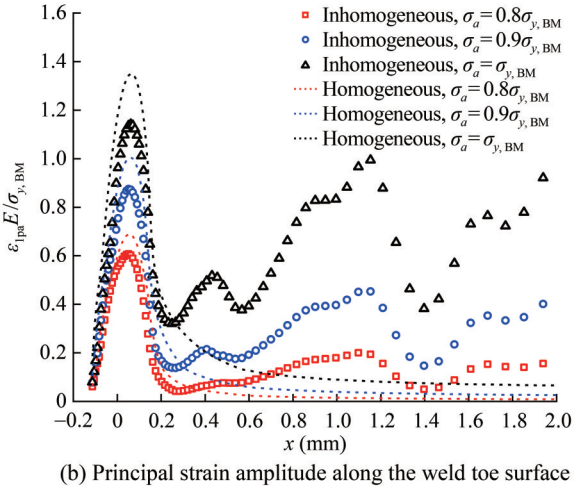

(b) Principal strain amplitude along the weld toe surface

Figure 9 Stress-strain response for the detailed inhomogeneous model and the homogeneous model

are also shown for comparison. Using the material properties of the crack initiation site, that is, the weld toe, to estimate the notch stress and strain of welded joints is a common practice. The material properties of the homogeneous model are derived based on the hardness of the measurement point near the weld toe, which is HV = 203.

Figure 9 shows that the maximum stress and strain appear at the notch for all the cases. For the inhomogeneous model, the principal stress amplitude generally decreases as the distance from the weld toe increases, ultimately approaching the amplitude of the remotely applied cyclic load. However, the principal plastic strain amplitude tends to increase with the distance from the weld toe after reaching a maximum at the weld toe arc. This behavior is consistent with the trend of smooth specimens, as shown in Figure 5(b). The aforementioned behavior can be attributed to the soft material. Some local fluctuations of the stress and strain are observed away from the weld toe due to material inhomogeneity, and the fluctuation increases with the applied cyclic load.

The location of the maximum principal stress amplitude is slightly different from that of the maximum principal plastic strain amplitude due to material inhomogeneity. The peak stress is observed around x = 0.1 mm, while the peak strain appears around x = 0.05 mm. Figure 7(b) shows that the hardness along the line of y = −0.1 mm increases from x = 0 mm to x = 0.5 mm. Consequently, the cyclic stress–strain curve shifts upward for the material from x = 0 mm to x = 0.5 mm. Therefore, despite the reduction in strain from x = 0.05 mm, the stress still increases.

For the homogeneous model, the maximum principal stress amplitude and the maximum principal plastic strain amplitude occur at the same location. Compared to the results from the inhomogeneous model, the maximum stress is underestimated, while the maximum strain is overestimated, with the deviation increasing as the applied cyclic load increases. A slight increase in the hardness enhances the consistency of the maximum values obtained from the two models because an increase in hardness can harden the material. This finding indicates that the material properties used in the homogeneous model should be carefully chosen to accurately predict the maximum stress and strain. Additionally, the homogenous model may underestimate the principal plastic strain amplitude at locations away from the weld toe, which highlights an inherent limitation of the model.

If the strain amplitude is used as the parameter for LCF assessment of welded joints, then a homogeneous model with material properties determined by the relatively low hardness measured near the weld toe may be employed. This approach facilitates an easy model construction and provides conservative results. Notably, the homogeneous model can only predict the stress and strain at the notch.

4.3 Simplifiled inhomogeneous model

The measured data are usually limited, and simplified inhomogeneous models are employed to estimate the notch stress and strain, which comprise several material zones

divided in accordance with the measured data. This section illustrates the performance of the simplified inhomogeneous model via comparison with the detailed inhomogeneous model.

A simplified inhomogeneous model based on the measured hardness at $y = -0.1$ is constructed. The hardness distribution along $y = -0.1$ is formulated using linear interpolation of measured data points. The shaded area in Figure 6(a) is divided into three material zones: $x = [-3\text{ mm}, -0.5\text{ mm}]$, $x = [-0.5\text{ mm}, 1\text{ mm}]$, and $x = [1\text{ mm}, 2.8\text{ mm}]$. The second material zone is further divided into material stripes with a width of 0.1 mm, as shown in Figure 10. The hardness of each zone or strip is calculated by averaging the hardness distribution in the zone or strip. The material properties of each zone or strip are determined in accordance with Section 2. The results are compared with those from the detailed inhomogeneous model, as shown in Figure 11.

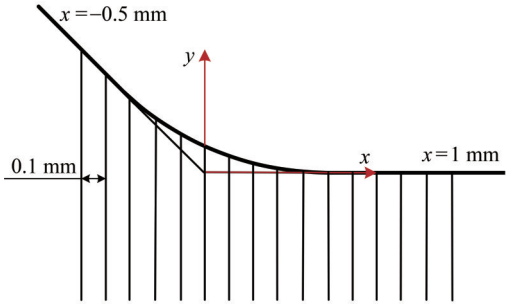

Figure 10 Material strips for the second zone

Compared to the results from the detailed inhomogeneous model, the simplified inhomogeneous model can accurately predict the maximum principal stress amplitude, while it underestimates the maximum principal plastic strain amplitude. The stress and strain at locations away from the weld toe are also underestimated, although the general trend is captured. This finding indicates that calibration of the simplified inhomogeneous model is still needed to obtain results that are consistent with those of the detailed inhomogeneous model. The effect of the strip width on the results is investigated, revealing that further reduction in width only has minimal effect. Another factor that may affect the results lies in the inclination of the strip. Figure 7(a) shows that the boundaries of the material zones are curved rather than straight lines. However, if only the measured hardness at $y = -0.1$ mm is available, determining the inclination of the material strips is difficult. The comparison between the detailed and simplified models indicates that the accuracy of the simplified inhomogeneous model, based on limited data, cannot be guaranteed.

The comparison results shown in Figures 9 and 11 indicate that both simplified models have limitations. The detailed inhomogeneous model provides a more accurate evaluation of the LCF performance of welded joints, which is valuable for the design of welded joints.

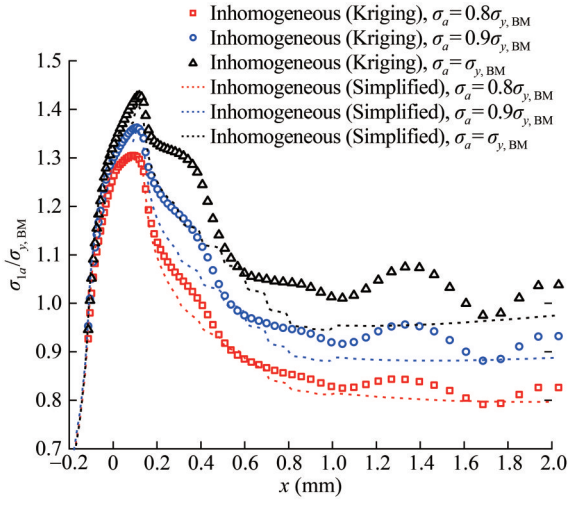

(a) Principal stress amplitude along the weld toe surface

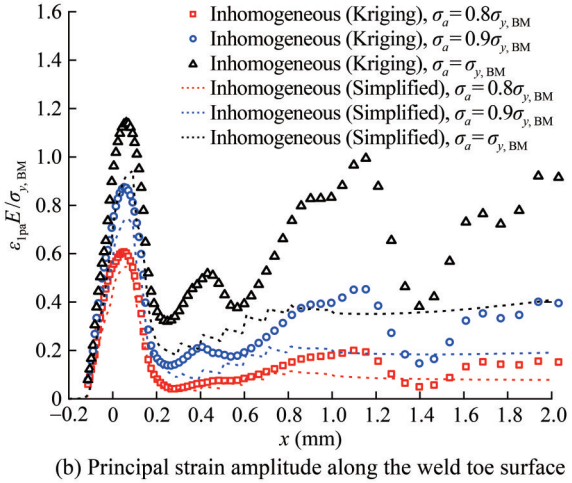

(b) Principal strain amplitude along the weld toe surface

Figure 11 Stress-strain response for the detailed and simplified inhomogeneous models

5 Fatigue life estimation

In this section, the fatigue life is estimated based on the local stresses and strains obtained in the previous sections. The SWT method, introduced in Section 2, is employed, where the fatigue properties are derived from the hardness. Figure 12 shows the strain-life curves for various hardness values, according to Eq. (9). A stress ratio is assumed to be −1. Therefore, the relationship between the principal strain amplitude and the maximum stress is given by Eq. (2). Notably, the fatigue life increases with hardness in the high-cycle fatigue regime, while it decreases in the low-cycle fatigue regime.

Figure 13(a) shows the fatigue life distribution along the smooth specimen surface (the number of HAZ subzones is 5). The load amplitude is $\sigma_{y,BM}$, and the load ratio is −1. Notably, the fatigue life distribution of the smooth specimen is generally opposite to the plastic strain amplitude distribution, as shown in Figure 5(b). A high plastic strain

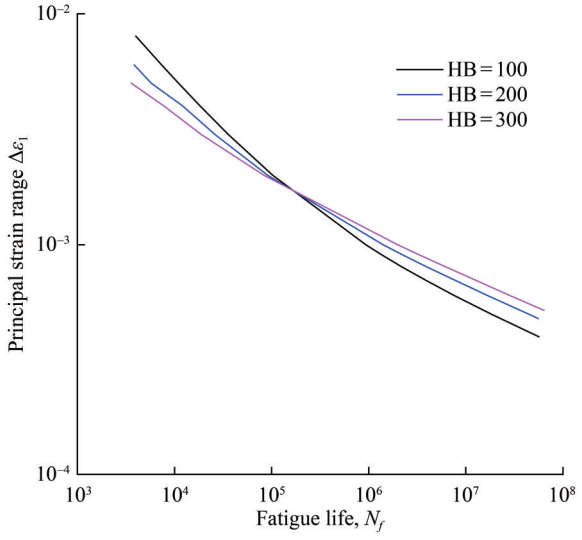

Figure 12 Strain-life curves for various values of hardness

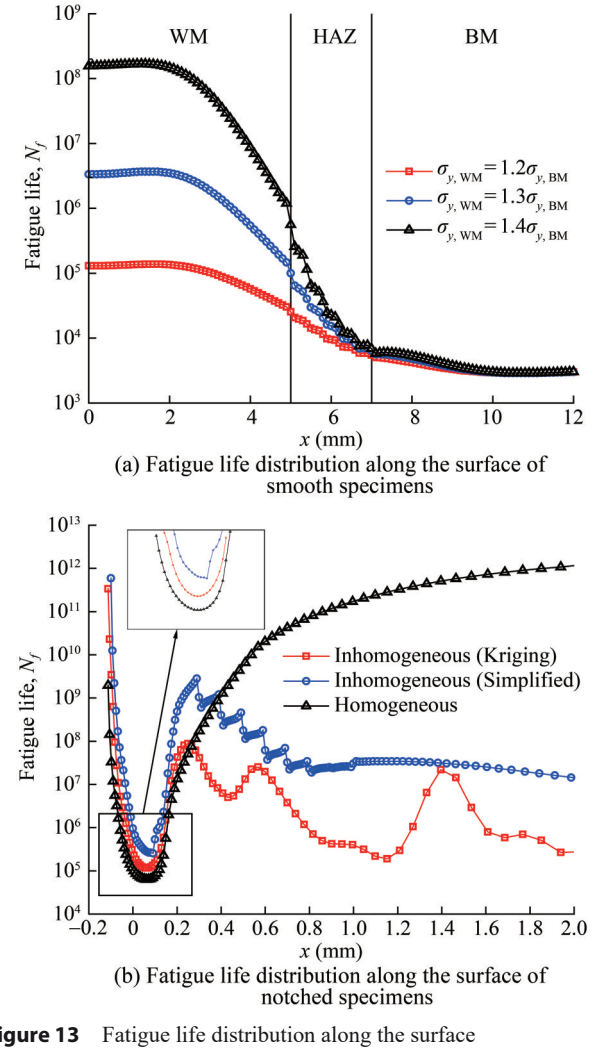

Figure 13 Fatigue life distribution along the surface

amplitude corresponds to a low fatigue life. Moreover, the fatigue life of WM increases with the mismatch ratio. If the effect of residual stress and the existence of defects are ignored, then the fatigue crack is more likely to be initiated at the BM a few millimeters away from the HAZ.

Figure 13(b) shows the fatigue life distribution along the notched specimen surface. Three finite element models analyzed in Section 4 are all evaluated. Notably, the fatigue life distribution is also opposite to the plastic strain amplitude distribution. The homogeneous model underestimates the fatigue life, while the simplified inhomogeneous model overestimates the fatigue life around the weld toe. The fatigue crack initiation location predicted by the simplified inhomogeneous model is slightly deviated from the location predicted by the other two models. The results indicate that the simplified homogeneous model should be further calibrated, and the homogeneous model, whose material properties are determined based on a relatively low hardness measured near the weld toe, may be more feasible in practice.

6 Conclusions

A numerical study on the effect of material inhomogeneity of welded joints on the local stress and strain was performed. Smooth specimens and welded joints with various material zones, whose material properties were determined based on their hardness, were analyzed under substantial monotonic or cyclic loading. The fatigue life was estimated using the SWT method. The following conclusions could be established:

1) Stress concentration and continuously increasing strain exist in the smooth specimen model with decreasing hardness distribution from WM to BM under significant monotonic and cyclic loads. The stress concentration occurs at a location where the strain is not significant and increases with the applied load and the mismatch ratio.

2) A detailed inhomogeneous model of a fillet welded T-joint is constructed based on intensive microhardness measurement around the weld toe and the Kriging interpolation method. In addition to the maximum stress and strain amplitude arising at the notch, the stress amplitude tends to decrease, and plastic strain amplitude tends to increase with the distance away from the notch. There are some local fluctuations in the stress and strain distribution due to material inhomogeneity.

3) The homogeneous model and the simplified inhomogeneous model based on limited measured data were analyzed, and their results were compared with those from the detailed inhomogeneous model. Significant deviations of the local strain exist when using the two simplified models. The homogeneous model can only predict the result of the notch, and the material properties should be carefully chosen. The simplified inhomogeneous model based on limited data cannot significantly improve the result, and

calibration of the model is still needed. A relatively low hardness measured close to the weld toe may be used to derive the material properties of the homogeneous model for a slight conservative strain amplitude estimation at the notch.

4) The fatigue life was estimated based on the local stresses and strain combining with the SWT method. The fatigue life is generally controlled by the plastic strain amplitude. For overmatched smooth specimen, the fatigue crack is more likely to be initiated from the BM a few millimeters away from the HAZ. The fatigue crack initiation location predicted by the simplified inhomogeneous model is slightly deviated from the location predicted by the other two models.

Funding Supported by the National Natural Science Foundation of China (52101350).

Competing interest Yan Dong is an editorial board member for the Journal of Marine Science and Application and was not involved in the editorial review, or the decision to publish this article. All authors declare that there are no other competing interests.

References

ANSYS (2012) Online Manuals

Basan R, Franulović M, Smokvina Hanza S (2010) Estimation of cyclic stress-strain curves for low-alloy steel from hardness. Metalurgija 49(2): 83-86. https://doi.org/10.1007/s12540-010-0427-7

Besel Y, Besel M, Dietrich E, Wischek J, Mercado UA, Kakiuchi T, Uematsu Y (2019) Heterogeneous local straining behavior under monotonic and cyclic loadings in a friction stir welded aluminum alloy. International Journal of Fatigue 125: 138-148. https://doi.org/10.1016/j.ijfatigue.2019.03.037

Dong Y, Garbatov Y, Guedes Soares C (2017) Fatigue strength assessment of an annealed butt welded joint accounting for material inhomogeneity. Progress in the Analysis and Design of Marine Structures 349-359. https://doi.org/10.1201/9781315157368-40

Dong Y, Teixeira A, Guedes Soares C (2020) Application of adaptive surrogate models in time-variant fatigue reliability assessment of welded joints with surface cracks. Reliability Engineering & System Safety 195: 106730. https://doi.org/10.1016/j.ress.2019.106730

Dong Y, Garbatov Y, Guedes Soares C (2022) Recent Developments in Fatigue Assessment of Ships and Offshore Structures. Journal of Marine Science and Application 21(4): 3-25. https://doi.org/10.1007/s11804-022-00301-x

Easterling K (2013) Introduction to the physical metallurgy of welding. Elsevier. https://doi.org/10.1016/C2013-0-04524-0

Ezer MA, Çam G (2022) A study on microstructure and mechanical performance of gas metal arc welded AISI 304 L joints. Materialwissenschaft und Werkstofftechnik 53(9): 1043-1052. https://doi.org/10.1002/mawe.202200050

Gaspar B, Teixeira AP, Guedes Soares C (2014) Assessment of the efficiency of Kriging surrogate models for structural reliability analysis. Probabilistic Engineering Mechanics 37: 24-34. https://doi.org/10.1016/j.probengmech.2014.03.011

Hobbacher A (2015) Recommendations for fatigue design of welded joints and components. Springer. https://doi.org/10.1007/978-3-319-23757-2

Kucharczyk P, Madia M, Zerbst U, Schork B, Gerwien P, Münstermann S (2018) Fracture-mechanics based prediction of the fatigue strength of weldments. Material aspects. Engineering Fracture Mechanics 198: 79-102. https://doi.org/10.1016/j.engfracmech.2017.09.010

Lopez Z, Fatemi A (2012) A method of predicting cyclic stress–strain curve from tensile properties for steels. Materials Science and Engineering 556: 540-550. https://doi.org/10.1016/j.msea.2012.07.024

Maddox SJ (1991) Fatigue strength of welded structures. Woodhead publishing

Madia M, Zerbst U, Beier HT, Schork B (2018) The IBESS model–Elements, realisation and validation. Engineering Fracture Mechanics 198: 171-208. https://doi. org/10.1016/j.engfracmech.2017.08.033

Mallieswaran K, Rajendran C, Padmanabhan R, Rajasekaran S (2023) Evaluation of nickel shot peening process on strength of friction stir welded AA2014-T6 aluminum alloy joints 60(7): 442-460. https://doi.org/10.1515/pm-2022-1038

Matheron G (1973) The intrinsic random functions and their applications. Advances in Applied Probability 5(3): 439-468. https://doi.org/10.2307/1425829

Paik JK, Sohn JM (2012) Effects of welding residual stresses on high tensile steel plate ultimate strength: nonlinear finite element method investigations. Journal of Offshore Mechanics and Arctic Engineering 134(2): 021401. https://doi.org/10.1115/1.4004510

Pavlina EJ, Van Tyne CJ (2008) Correlation of Yield Strength and Tensile Strength with Hardness for Steels. Journal of Materials Engineering and Performance 17(6): 888-893. https://doi.org/10.1007/s11665-008-9225-5

Radaj D, Sonsino CM, Fricke W (2006) Fatigue assessment of welded joints by local approaches. Woodhead publishing

Rajendran C, Ben Ruben R, Ashokavarthanan P, Mallieswaran K (2022) Identifying the Effect of PWHT on Strength of Laser Beam Welding Joints of AA2024 Aluminum Alloy. ASME Open Journal of Engineering, 1. https://doi.org/10.1115/1.4053496

Remes H (2008) Strain-based approach to fatigue strength assessment of laser-welded joints. Ph. D. thesis Helsinki University of Technology

Remes H, Varsta P, Romanoff J (2012) Continuum approach to fatigue crack initiation and propagation in welded steel joints. International Journal of Fatigue 40: 16-26. https://doi.org/10.1016/j.ijfatigue.2012.01.007

Roessle M, Fatemi A (2000) Strain-controlled fatigue properties of steels and some simple approximations. International Journal of Fatigue 22(6): 495-511. https://doi.org/10.1016/S0142-1123(00)00026-8

Saiprasertkit K, Hanji T, Miki C (2012) Fatigue strength assessment of load-carrying cruciform joints with material mismatching in low-and high-cycle fatigue regions based on the effective notch concept. International Journal of Fatigue 40: 120-128. https://doi.org/10.1016/j.ijfatigue.2011.12.016

Şenol M, Çam G (2023) Investigation into microstructures and properties of AISI 430 ferritic steel butt joints fabricated by GMAW. International Journal of Pressure Vessels and Piping: 202: 104926. https://doi.org/10.1016/j.ijpvp.2023.104926

Serindağ HT, Çam G (2022) Multi-pass butt welding of thick AISI 316L plates by gas tungsten arc welding: Microstructural and mechanical characterization. International Journal of Pressure

Vessels and Piping 200: 104842. https://doi.org/10.1016/j.ijpvp.2022.104842

Serindağ HT, Tardu C, Kirçiçek İÖ, Çam G (2022) A study on microstructural and mechanical properties of gas tungsten arc welded thick cryogenic 9% Ni alloy steel butt joint. CIRP Journal of Manufacturing Science and Technology 37: 1-10. https://doi.org/10.1002/mawe.202200050

Serindağ HT, Çam G (2023) Characterizations of Microstructure and Properties of Dissimilar AISI 316L/9Ni Low-Alloy Cryogenic Steel Joints Fabricated by Gas Tungsten Arc Welding. Journal of Materials Engineering and Performance 32(15): 7039-7049. https://doi.org/10.1007/s11665-022-07601-x

Serindağ HT, Çam G (2021) Microstructure and mechanical properties of gas metal arc welded AISI 430/AISI 304 dissimilar stainless steels butt joints. Journal of Physics: Conference Series 1777(1): 012047. https://doi.org/10.1088/1742-6596/1777/1/012047

Smith K (1970) A stress-strain function for the fatigue of metals. Journal of materials, 5, 767-778

Tsutsumi S, Fincato R, Luo P, Sano M, Umeda T, Kinoshita T, Tagawa T (2022) Effects of weld geometry and HAZ property on low-cycle fatigue behavior of welded joint. International Journal of Fatigue 156: 106683. https://doi.org/10.1016/j.ijfatigue.2021.106683

Venkataramanan AR, Dhanenthiran M, Balasubramanian K, Mallieswaran K, Vinosh M (2022) Predict the fatigue life of solution treated and aged TIG welded AA6061 aluminum alloy joints. AIP Conference Proceedings 2527(1): 020020. https://doi.org/10.1063/5.0108128

Wang R, Shang D (2009) Low-cycle fatigue life prediction of spot welds based on hardness distribution and finite element analysis. International Journal of Fatigue 31(3): 508-514. https://doi.org/10.1016/j.ijfatigue.2008.04.009

Wang Y, Fincato R, Morita K, Wang Q, Tsutsumi S (2023) Cyclic elastoplasticity-based life assessment of fatigue crack initiation and subsequent propagation in rib-to-deck welded joints. International Journal of Fatigue 107679. https://doi.org/10.1016/j.ijfatigue.2023.107679

Xu Z, Zhang J, Zhu B (2022) Low cycle fatigue properties of a 9–12% Cr martensitic steel welded joint with Ni-based weld metal based on a local strain approach. Engineering Failure Analysis 138: 106347. https://doi.org/10.1016/j.engfailanal.2022.106347

Yao Z, Omiya M, Ma N, Nishi S, Takada K, Okato K, Oide K, Kobayashi T, Han J, Terada K (2023) Local mechanical characterization and fracture prediction modeling for resistance spot-welded joints of advanced high-strength steel. Materials Today Communications 36. https://doi.org/10.1016/j.mtcomm.2023.106787